NANO LETTERS

Letter

pubs.acs.org/NanoLett

Tailoring the Energy Landscape in Quasi-2D Halide Perovskites Enables Efficient Green-Light Emission

Li Na Quan,[†,‡] Yongbiao Zhao,[§] F. Pelayo García de Arquer,[†] Randy Sabatini,[†] Grant Walters,[†] Oleksandr Voznyy,[†] Riccardo Comin,[†] Yiying Li,[§] James Z. Fan,[†] Hairen Tan,[†] Jun Pan,[∥] Mingjian Yuan,[†] Osman M. Bakr,[∥] Zhenghong Lu,[*,§] Dong Ha Kim,[*,‡] and Edward H. Sargent[*,†]

[†]Department of Electrical and Computer Engineering, University of Toronto, 10 King's College Road, Toronto, Ontario M5S 3G4, Canada

[‡]Department of Chemistry and Nano Science, Ewha Woman's University, 52 Ewhayeodae-gil, Seodaemun-gu, Seoul 03760, Korea

[§]Department of Materials Science and Engineering, University of Toronto, 184 College Street, Toronto, Ontario M5S 3E4, Canada

[∥]Division of Materials Science and Engineering, King Abdullah University of Science and Technology, Thuwal 23955-6900, Kingdom of Saudi Arabia

S *Supporting Information*

ABSTRACT: Organo-metal halide perovskites are a promising platform for optoelectronic applications in view of their excellent charge-transport and bandgap tunability. However, their low photoluminescence quantum efficiencies, especially in low-excitation regimes, limit their efficiency for light emission. Consequently, perovskite light-emitting devices are operated under high injection, a regime under which the materials have so far been unstable. Here we show that, by concentrating photoexcited states into a small subpopulation of radiative domains, one can achieve a high quantum yield, even at low excitation intensities. We tailor the composition of quasi-2D perovskites to direct the energy transfer into the lowest-bandgap minority phase and to do so faster than it is lost to nonradiative centers. The new material exhibits 60% photoluminescence quantum yield at excitation intensities as low as 1.8 mW/cm^2, yielding a ratio of quantum yield to excitation intensity of 0.3 cm^2/mW; this represents a decrease of 2 orders of magnitude in the excitation power required to reach high efficiency compared with the best prior reports. Using this strategy, we report light-emitting diodes with external quantum efficiencies of 7.4% and a high luminescence of 8400 cd/m^2.

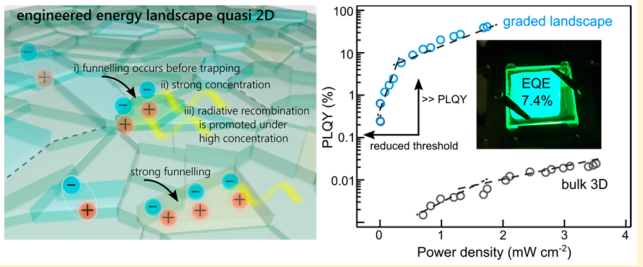

KEYWORDS: *Perovskites, Quasi-2D perovskites, Light-emitting diodes, photoluminescence quantum yield, energy transfer, Monte Carlo*

Organo-metal halide perovskites (OHP) have emerged as a new class of optoelectronic materials for solar cells,[1−3] optically pumped lasers,[4−6] and light-emitting diodes (LEDs).[7−12] However, their low exciton binding energy,[13−15] as well as their high electron and hole mobilities, lead to poor photoluminescence quantum yields (PLQYs) at low-excitation regimes.[16] To attain useful PLQYs, high-excitation photon fluences must be supplied, and this ultimately results in compromised photostability that limits light-emission applications.[17]

Organic−inorganic hybrid perovskites have an ABX_3 three-dimensional (3D) lattice framework that, through ion modification, can be spectrally tuned.[18] The low exciton binding energy in these systems results in a free-charge character in crystalline domains that slows radiative recombination.[15] Exciting the materials into a high-injection regime is required to attain moderate light-emission efficiency. This, on top of the limited stability of these materials,[19] can produce unstable operation and fast degradation in light-emitting applications.[20]

In contrast, lower dimensionality organic−inorganic hybrid perovskites are characterized by inorganic layers spaced using organic ligands.[21] This provides an excellent combination of structural and photophysical properties, such as the ability to tune the material bandgap depending on the dimensionality,[22,23] increased exciton binding energy, and higher stability compared with 3D counterparts.[19] Depending on the number of perovskite layers sandwiched between the organic linkers, these type of OHPs are termed 2D (e.g, a single $PbBr_2$ layer) or quasi-2D (a distribution of layers with different thicknesses) perovskites.

Low-dimensional perovskites are particularly attractive for visible light-emission applications, and LEDs based on quasi-2D perovskites have been actively explored. However, these devices show low efficiency (below 1%).[24,25]

Received: March 7, 2017
Revised: April 27, 2017
Published: May 5, 2017

DOI: 10.1021/acs.nanolett.7b00976
Nano Lett. XXXX, XXX, XXX−XXX

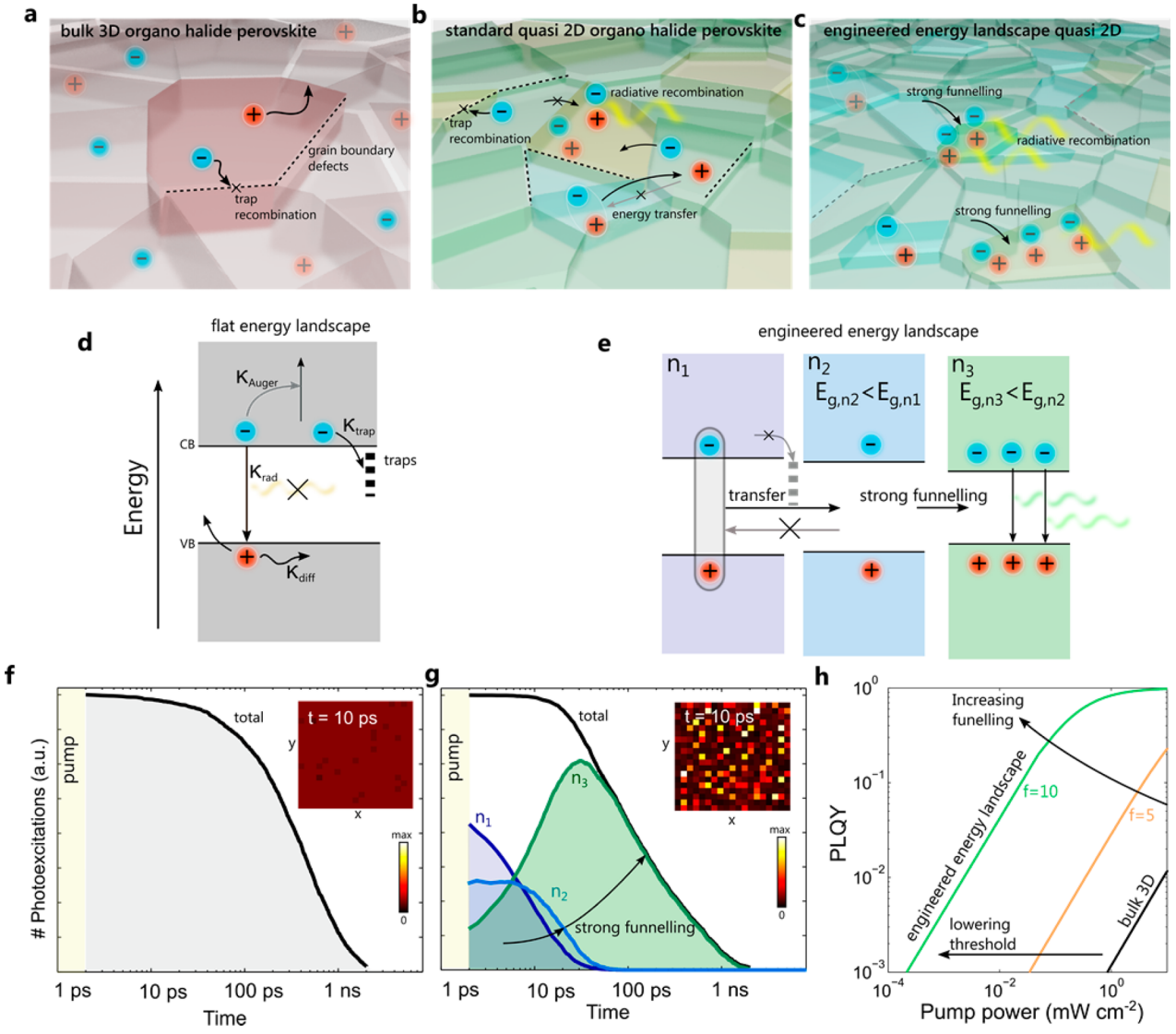

Figure 1. Tailoring the energy landscape in quasi-2D halide perovskites for efficient light emission. (a) In bulk-3D perovskites, the high diffusivity of charges militate against radiative recombination. (b) In quasi-2D perovskites, free charges and excitons coexist. A competition between radiative and nonradiative recombination exists, determined by the density of defects and on the density of photoexcited charges and excitons. (c) In energy-landscape-engineered quasi-2D perovskites, energy funnelling occurs faster than nonradiative recombination. As a consequence, photoexcited states are strongly concentrated in a subpopulation of domains, thereby increasing the probability of bimolecular radiative recombination. (d) In a flat-energy-landscape material, charges can either be trapped (with a rate of k_{trap}) or lost via Auger (k_{Auger}) or radiative (k_{rad}) recombination. The presence of trap states within, and at the boundaries, of the different grains, results in significant nonradiative recombination. (e) This limiting process can be overcome provided energy is funnelling to lower-bandgap domains before nonradiative recombination occurs. (f) Monte Carlo simulation of the time evolution of photoexcited states after pumping in a flat-energy-landscape system. Inset: distribution of excited states within the organohalide perovskite matrix after the initial 10 ps. After the initial excitation, only trapping events are recorded. (g) In energy-landscape-engineered systems, energy transfer outcompetes nonradiative processes. The photoexcited states are fully transferred from n_1 to n_2 and n_3 domains within the first 100 ps. Inset: distribution of excited states after the initial 10 ps. An increasing contribution of radiative events is recorded upon exciton funnelling (Figure S1). (h) The strong energy concentration in energy-landscape-engineered quasi-2D systems enables a high PLQY at much lower pump intensities.

The radiative properties of quasi-2D perovskite systems based on $PEA_2(MA)_{n-1}Pb_nI_{3n+1}$ (phenylethylammonium, PEA; CH_3NH_3, MA, methylammonium) have recently been reported for near-infrared LED applications.[26] The dimensionality of this material was tuned by varying the ratio of methylammonium iodide (MAI) to PEAI. This created a distribution of domains with varying numbers of perovskite layers centered on an average value $< n >$. An impressive PLQY enhancement was achieved in the low-$< n >$ regime. This was attributed to an inhomogeneous energy landscape that favored funnelling of energy into domains with lower bandgap (higher dimensionality). A quantitative model of this phenomenon, together with a design strategy to unlock further advances in performance, remains to be reported.

Herein, we demonstrate the prerequisites for an efficient energy-funnelling mechanism that gives rise to high PLQYs in quasi-2D perovskite systems. We find that only when energy is funnelling from high bandgap domains into a small subpopulation of lower bandgap domains does radiative recombination outcompete nonradiative recombination. Only

DOI: 10.1021/acs.nanolett.7b00976
Nano Lett. XXXX, XXX, XXX−XXX

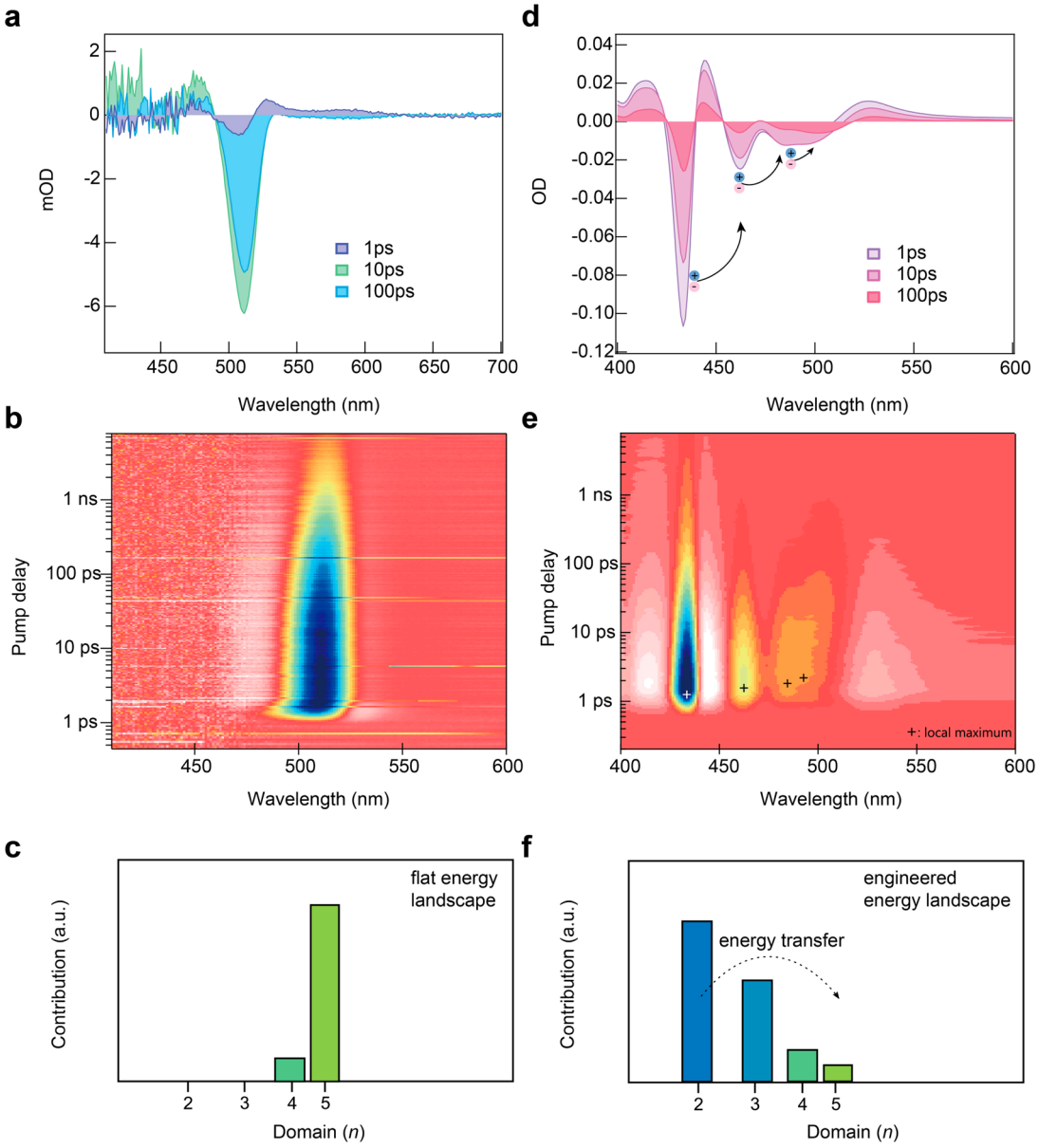

Figure 2. Controlling the energy landscape for quasi-2D perovskites through the crystallization process. Transient absorption spectra of (a–c) flat and (d–f) energy-landscape-engineered $< n \geq 3$ quasi-2D perovskite films. The relative presence of different n domains was extracted from the amplitude of the ground-state bleach peaks (see the Materials and Methods section). In the case of a flat energy landscape, $n = 5$ dominates. Energy-landscape-engineered films instead consist of a set of different domains where energy funnels into the final $n = 5$ domain.

then does the high charge concentration in these domains modulate charge-recombination kinetics. In particular, we found that the distribution of these domains is crucial for achieving high PLQY and LED performance.

Based on these findings, we then developed a fabrication strategy to control the domain distribution in quasi-2D perovskites. Specifically, we modulate the domain distribution in $PEA_2(MA)_{n-1}Pb_nBr_{3n+1}$ perovskites through their composition and solvent engineering during crystallization. In agreement with the model, only when the quasi-2D films are composed of a distribution of different bandgap domains does highly efficient light emission occur.

The energy-landscape-engineered quasi-2D perovskite system exhibits high photoluminescence yields at remarkably low excitation intensities (60% at 1.8 mW/cm^2, corresponding to a ratio of quantum yield to excitation intensity of 0.3 cm^2/mW). This represents an over two-orders-of-magnitude decrease in the excitation density at which the quantum yield rises above the 50% mark when compared with previously reported solution-processed perovskite PLQYs.

Using these materials, we fabricated LED devices with external quantum efficiencies (EQEs) of 7.4% accompanied by high luminescence brightness (8400 cd/m^2). These also feature notable improvements in stability compared with conventional $MAPbBr_3$ perovskites.

Results and Discussion. In conventional bulk 3D perovskites (Figure 1a), excited charges diffuse faster than they recombine radiatively, ultimately becoming trapped at grain boundary defects. In lower dimensional systems, such as quasi-2D OHPs, a combination of free charges and excitons coexist in smaller grains, which increases the radiative recombination probability compared to the bulk-3D scenario

DOI: 10.1021/acs.nanolett.7b00976
Nano Lett. XXXX, XXX, XXX–XXX

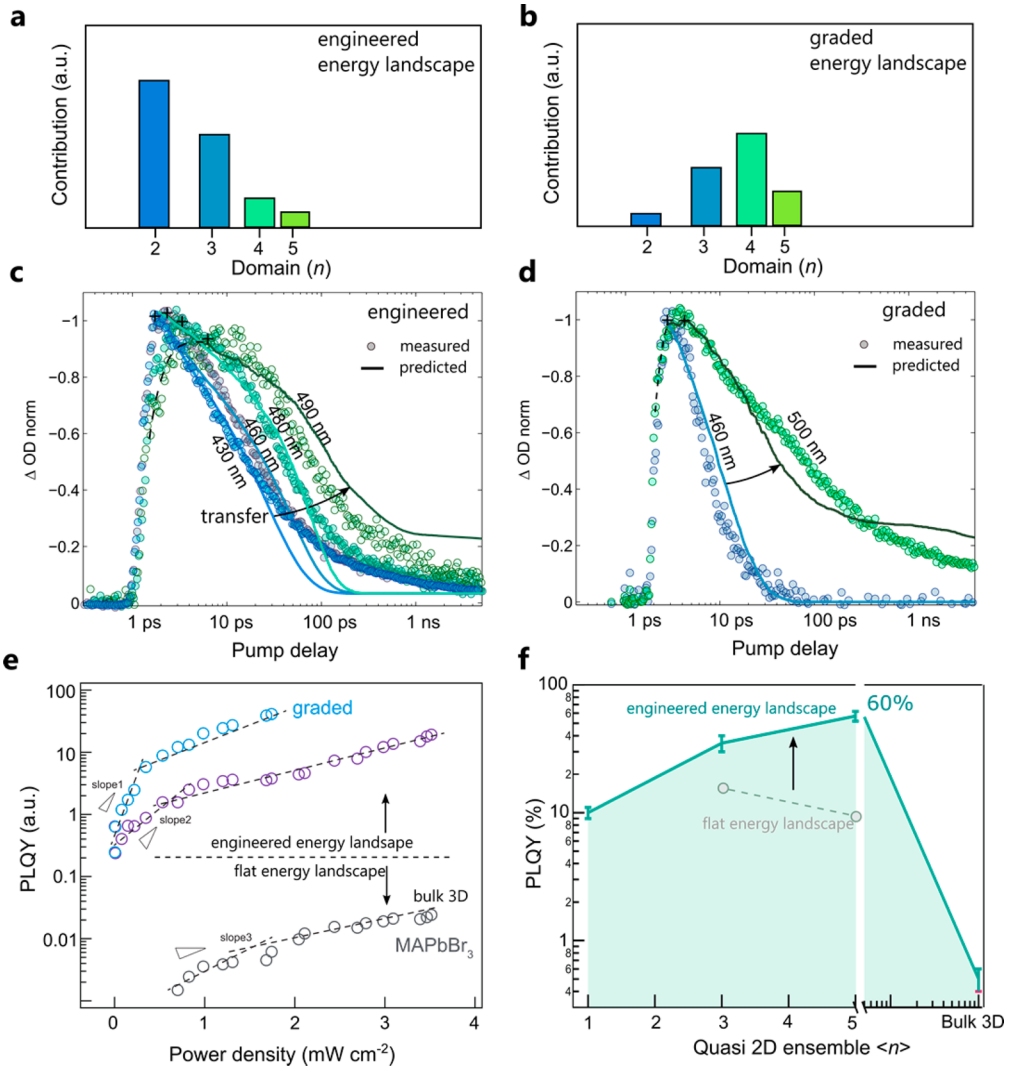

Figure 3. Optimizing energy transfer in energy-landscape-engineered quasi-2D perovskite systems. (a–d) Contribution of different domains in energy-landscape-engineered and graded-energy-landscape quasi-2D perovskite films as estimated from transient absorption spectroscopy (c,d) Experimental and predicted time-dependent transient absorption traces for engineered $< n \geq 3$ (c) and graded $< n \geq 5$ (d) films for different wavelengths. (e) PLQY as a function of pump power density for different material systems, showcasing the benefits of energy-landscape-engineered quasi-2D perovskites. (f) PLQY for different quasi-2D perovskite configurations.

(Figure 1b). However, surface and interface defects can still dominate because of the smaller grain sizes and the extended interfaces.[27,28] We hypothesized that, if the energy landscape in this material system was modulated in such a way that energy transfer could be fast enough to outpace trapping and subsequent nonradiative recombination, photoexcited states would be concentrated in small radiative domains, in which bimolecular radiative recombination would be enhanced because of the higher concentration (Figure 1c). This would in turn result in high luminescence yields, even in low-injection regimes.

To gain insight into the conditions under which energy transfer is sufficient to enhance radiation efficiency, we developed a stochastic Monte Carlo model that accounted for charge recombination and transfer processes (Figure 1d,e and the Supporting Information). The dynamics of the excited population (N), following impulsive photoexcitation, can be described by the rate equation:

$$\frac{dN}{dt} = -N(A + BN + CN^2) + \phi(t) \quad (1)$$

where A, B, and C are material-specific coefficients related, respectively, to Shockley–Read–Hall (trap) recombination (1st order), bimolecular photoluminescence (2nd order), and Auger recombination (3rd order). $\phi(t)$ represents the rate of exciton generation per volume.[29]

We first modeled the energy transfer and recombination yield of a flat energy landscape material (Figure 1f and the Supporting Information). Under these conditions we observe no preferential energy accumulation (Figure 1f inset), and, as a consequence, trapping becomes the dominant loss mechanism.

Energy-landscape-engineered multidomain materials, however, display a significantly different behavior (Figure 1g). For example, in a ternary system consisting of $< n > = \{n_1, n_2, n_3\}$ (see the Supporting Information for details), excitons sequentially funnelling from higher- to lower-bandgap domains, ultimately concentrating in final acceptor domains (n_3) (Figure 1g inset). In this scenario, photon emission outcompetes trapping within the initial 10 ps (Figure S10) as the strong

DOI: 10.1021/acs.nanolett.7b00976
Nano Lett. XXXX, XXX, XXX–XXX

Table 1. TA (Experimental) Lifetime

	$< n \geq 3$				$< n \geq 5$	
	430 nm	460 nm	480 nm	490 nm	460 nm	500 nm
1st exponential	5.7 ps	16 ps	30.7 ps	70.5 ps	3.5 ps	6.07 ps
2nd exponential	42 ps	198 ps	169 ps	1 ns	26 ps	3 ns

Table 2. PLQY, Pump Power (P_{pump}), and PLQY-to-P_{pump}

reference	year	regime	PLQY (%)	P_{pump} (mW cm^{-2})	PLQY/ P_{pump}	perovskite
15	2014	NIR	50	100	0.005	$MAPbI_xCl_{3-x}$
7	2014	NIR	26	333	0.00078	$MAPbI_xCl_{3-x}$
7	2014	visible	7	–	–	$MAPbBr_3$
10	2015	visible	36	1000	0.00036	$MAPbBr_3$
flat energy landscape (this work)	2016	visible	12	1.8	0.06	$PEA_2(MA)_4Pb_5Br_{16}$
engineered landscape (this work)	2016	visible	60	1.8	0.33	$PEA_2(MA)_4Pb_5Br_{16}$

charge concentration favors bimolecular radiative recombination (eq 1).

This downward energy cascade is expected to reduce the typically high optical pump powers and driving voltages required for efficient light emission in OHP systems due to the improved radiative efficiency. This is revealed by the computed PLQY as a function of pump power intensity in different materials systems (Figure 1h). Depending on the concentration coefficient f, where f denotes the effective increase of charge density in the final radiative domains compared to a flat-energy-landscape scenario, we observe a two orders-of-magnitude reduction in the pump power required to achieve high PLQY as f increases from 1 to 10. We conclude that energy funnelling in engineered landscapes can be exploited to improve the radiative properties of otherwise nonideal materials, leading to efficient light emission achievable at lower driving powers.

With these concepts in mind, we sought to define experimentally the energy landscape and energy flow dynamics in different OHP material systems. We synthesized quasi-2D bromide perovskites $PEA_2(MA)_{n-1}Pb_nBr_{3n+1}$ at a judiciously selected stoichiometry (Figure S1).[19,26] We employed different antisolvents to control perovskite formation in a fast crystallization single-step spin-coating method.[30] We took the view that the different boiling point of toluene (110 °C) and chloroform (61 °C) would result in different crystallization kinetics and resulting domain distributions. The high boiling point of toluene would favor the formation of more-uniform domains (flat energy landscape), whereas chloroform, with faster evaporation, would lead to the formation of smaller clusters with different bandgaps (Figures S3 and S4).

We used ultrafast transient absorption spectroscopy (TA) measurements, to monitor the dynamics of energy transfer and thereby reveal the differences between these material configurations (Figure 2). In the case of the flat energy landscape of standard quasi-2D perovskites, no energy migration is observed. A single bleach decay is recorded that coincides with the ground-state bleach (GSB) and the excitonic peak obtained by linear absorption measurements (Figure 2a,b). The extracted domain distribution is, in this case, dominated by a single domain component (Figure 2c).

Energy-landscape-engineered perovskites behave quite differently (Figure 2d–f). Several GSBs are observed, and the decay kinetics of the different GSB peaks correlate well with the notion of energy transfer.[31] The GSB maxima are sequentially delayed for lower-energy features, indicative of domains that receive charges from (larger bandgap) domains. The energy transfer is observable in the first 10 ps, after which these points correspond, for each domain, to the time at which the population in each lower domain decays faster than it grows from energy funnelling. The decay kinetics are slower for lower energy features (acceptor domains). These facts together indicate that energy is funnelling from wider to narrower bandgap grains. The extracted domain distribution is in this case composed of a set of components with different bandgaps that favor energy concentration into the emitting domain (Figure 2e). Signatures of energy transfer in landscape-engineered perovskites are also evident in time-resolved PL emission studies, which show ultrafast (ps) and slow (ns) transfer components (Figure S9).

We then sought to apply our Monte Carlo model to fit the energy-transfer kinetics in different landscape-engineered configurations to provide insights into the rates of the different processes involved (Figure 3a). The different rise, maxima, and fall times for the various GSBs are evidence of energy transfer between the different domains, which are in good agreement with the theoretical predictions. Our model elucidates transfer rates on the order of ps^{-1} between the different perovskite domains and estimates the instantaneous contributions of radiative, trap, and Auger mechanisms (Figure S10). Photoexcited states' lifetimes are shorter in wider-bandgap grains, as these are the most likely to be transferred to narrower-bandgap grains over ∼10 ps (Table 1).

With these findings in mind, we then sought to further improve the final radiative efficiency and therefore pursued control of the distribution of the different domains. We took the view that optimizing the concentration of the $n = 5$ emitting domains would allow a more-efficient, graded funnelling, wherein the majority of the charges are concentrated in $n = 5$ domains rather than trapped or emitted in higher-bandgap clusters before concentration.

To do so, we reduced the quantity of organic PEABr and MABr ligands involved in the perovskite synthesis, seeking to promote the formation of $n = 5$ domains. As revealed by transient absorption, the resulting films exhibited a different, broader distribution of n domains with a higher $n = 5$ contribution (Figure S8). We input the extracted domain distribution into our model, which yields good agreement with the experimental TA decay traces (Figure 3b). The decay kinetics reveal a faster charge injection from the donor to the acceptor domains, which we attribute to the more graded

DOI: 10.1021/acs.nanolett.7b00976
Nano Lett. XXXX, XXX, XXX−XXX

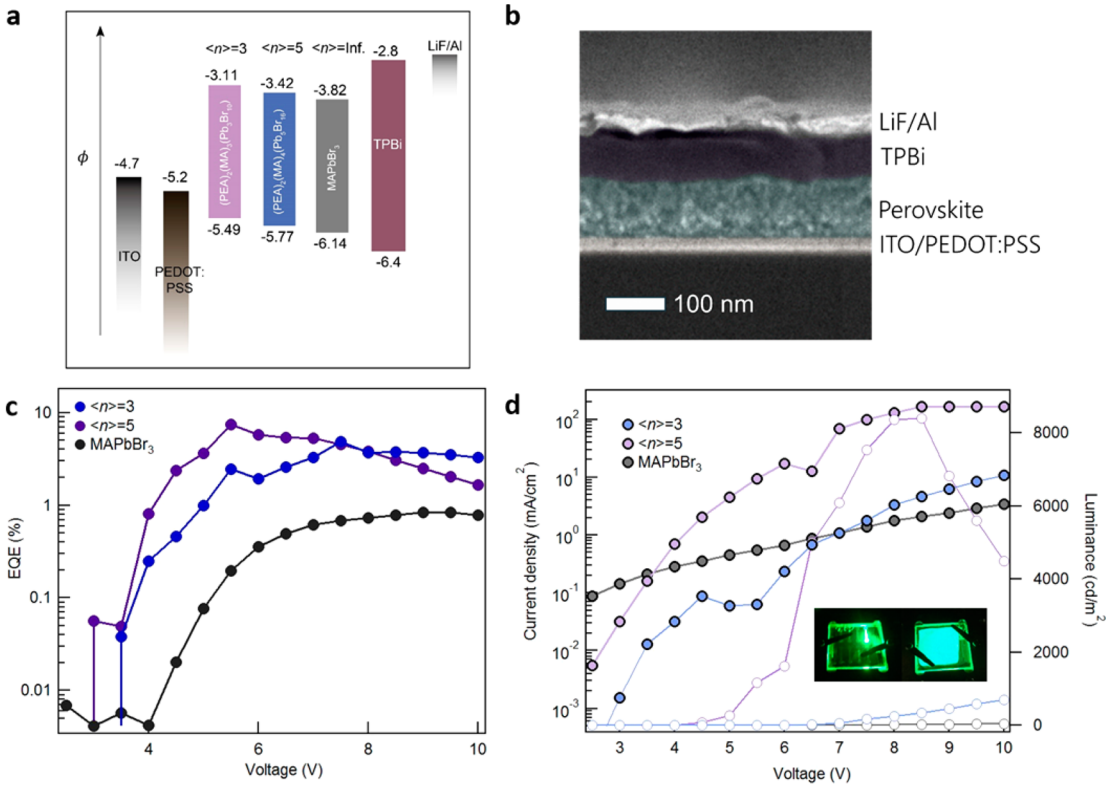

Figure 4. Energy-landscape-engineered quasi-2D perovskites for highly efficient LEDs. (a) Band structure of perovskites with different perovskites and energy-band alignment of LED device. (b) Cross-sectional SEM image of an LED device (artificially colored). (c) EQE vs applied voltage characteristics of the device with different perovskites. (d) Summary of the *J*–*V*–*L* characteristics in different-perovskites-based devices.

domain distribution that increases the probability of sequential energy transfer.

We then sought to assess experimentally how efficient energy transfer could lower the power at which high PLQY could be attained and studied PLQY as a function of pump power for the different types of perovskite systems (Figure 3c). As predicted, energy-landscape-engineered quasi-2D perovskites show a substantially higher PLQY compared with flat-landscape, bulk ($MAPbBr_3$), and PEA_2PbBr_4 (2D) perovskites (Figure S7).

Graded landscape $< n \geq 5$ perovskites show a prominent PLQY of ~60% at an excitation power density as low as 1.8 mW/cm^2 (Figure 3d). This yields a PLQY to pump power density ratio of 0.3 cm^2/mW, a two-orders-of-magnitude improvement over prior perovskite systems (Table 2).

We then translated the low operating powers of refined landscape-engineered quasi-2D perovskite materials into LED applications and built LED devices employing $< n \geq 3$ (engineered landscape), $< n \geq 5$ (graded optimized landscape), and bulk $MAPbBr_3$ (flat landscape) photoactive layers (Figure 4a). Cross-sectional SEM indicates the presence of two uniform layers: a hole-injection layer of PEDOT/PSS (Al4083) (~10 nm) coated with a dense perovskite emitter layer (~130 nm). A total of 100 nm of TPBi was coated to provide an electron injection layer, followed by a LiF/Al (1/100 nm) electrode on top (Figure 4b). Under forward bias, electrons and holes are injected from the cathode—electron injection layer (TPBi) and anode—hole-injection layer (PEDOT/PSS), respectively, and are efficiently transferred to the perovskite, where they concentrate into the emitting domains to recombine radiatively. Ultraviolet photoemission spectroscopy (UPS) measurements were also performed to determine the valence band position and work function of the resulting perovskites (Figure 6).

Flat landscape bulk perovskite devices exhibit low performance with a 0.8% EQE and 33.7 cd/m^2 luminance (Figure 4c and d). This is expected in view of their lower PLQY (Figure 3f). Devices based on landscape-engineered quasi-2D perovskites, however, show improved optoelectronic characteristics. $< n > = 3$ devices exhibit reduced turn-on voltages and an order-of-magnitude increase in EQE and luminance (up to 4.8% and 1000 cd/m^2) (Figure 4c and d). Graded $< n \geq 5$ devices display a significant enhancement in EQE (7.4%) and luminance (8400 cd/m^2) (Figures S11 and S13). The EL spectra of these devices closely match the PL spectra, preserving a narrowband emission (Figure S12). Large area devices (6.54 cm^2) based on graded $< n > = 5$ perovskites were also fabricated (Figure 4d inset) and show high brightness with strong optical uniformity. The low device operational stability may due to the material photostability and interaction of perovskite with the device interfacial layers (Figure S14).

Conclusions. We demonstrated the conditions required for efficient radiative recombination in low-dimensional perovskite systems. We found that when the energy landscape in the perovskite is modulated in such a way that energy transfer outpaces nonradiative recombination, concentrating charges into a subpopulation of radiative domains, efficient light emission take place. We devised a perovskite synthesis and crystallization method whereby domain distribution could be controlled. By optimizing the domain distribution, we achieved a record PLQY of 60% at low excitation fluences (1.8 mW/cm^2) for solid films at green wavelengths. This represents the highest maximum yield-to-driving-power reported for organometal halide perovskite materials (0.3 cm^2/mW). We translated these findings into LED devices with high EQEs (7.4%) and high luminescence (8400 cd/m^2) at low threshold voltages.

DOI: 10.1021/acs.nanolett.7b00976
Nano Lett. XXXX, XXX, XXX−XXX

Materials and Methods. *Perovskite Film Fabrication.* The quasi-2D and $MAPbBr_3$ perovskites precursors were prepared by dissolving specific stoichiometric quantities of lead bromide ($PbBr_2$, 99.98% Alfa-Aesar), methylammonium bromide (MABr, Dyesol), and phenylethylammonium bromide (PEABr, Dyesol) in dimethyl sulfoxide (DMSO) solvent. The resulting solution was filtered using a polytetrafluoroethylene syringe filter (0.2 μm) before deposition. The precursor solution was coated onto the substrate via a consecutive two-step spin coating process at 1000 and 5000 rpm for 10 and 60 s, respectively. During the second spin step, 100 μL of chloroform (or toluene) was deposited onto the substrate. The resulting films were then annealed at 90 °C for 5 min for better crystallization.

Moreover, the time of dripping antisolvent (before the evaporation of DMSO) is essential to get high-quality and better-crystallized film. To assess the crystal structure and layered nature of the resulting films, we measured film X-ray diffraction (XRD) of pure-phase $MAPbBr_3$ and quasi-2D perovskites with $< n > = 3$ and $< n > = 5$ (Supplementary Figure 2). The XRD patterns of $MAPbBr_3$ films reveal Bragg reflections at 15.23° and 30.44° that can be indexed to the (100) and (200) planes. This indicates a high-purity cubic phase of $MAPbBr_3$ perovskite. Signatures of layered perovskite structure were obtained at low-diffraction angles ($2\theta < 10°$) in $< n > = 3$ perovskite films. Similar reflection patterns for $< n > = 5$ and $MAPbBr_3$ indicate a preferential orientation of the grains on the substrate. Interestingly, quasi-2D perovskites with $< n > = 3$ and $< n > = 5$ show extremely small grain sizes, on the order of 10 nm, and high smoothness, below 10 nm rms. $MAPbBr_3$ perovskites, however, consistently present larger grains (>50 nm) and high surface roughness (above 50 nm rms) (Supplementary Figure 3). Grain sizes calculated from XRD peaks full width at half-maximum are consistent with AFM results.

Light-Emitting Diode Fabrication. A PEDOT/PSS (Clevios PVP Al4083) layer was spin-coated on oxygen-plasma-treated patterned ITO-coated glass substrates and then annealed on a hot plate at 150 °C for 20 min in air. Perovskite precursor solutions were spin-coated onto the PEDOT/PSS via the two-step fast crystallization spin-coating method that was described above. TPBi (100 nm) and LiF/Al electrodes (1 nm/100 nm) were deposited using a thermal evaporation system through a shadow mask under a high vacuum of less than 10^{-4} Pa. The device active area was 12.2 mm^2 as defined by the overlapping area of the ITO and Al electrodes. Unpatterned ITO substrates (1 in. by 1 in.) were used for the large-area devices. All devices were tested under ambient conditions with encapsulated devices.

AFM Measurements. Atomic force microscopy (AFM) was used to characterize sample morphology. An Asylum Research Cypher AFM was operated in AC mode in air to obtain topographical and phase images. ASYELEC-02 silicon probes with titanium−iridium coatings from Asylum Research were used for all imaging. The typical spring constant of the probes is 42 N/m.

XRD Measurements. XRD measurement on oriented films were conducted on a Panalytical X'Pert Pro diffractometer with a Bragg−Brentano geometry and PLXCEL 1D detector equipped with a nickel filter.

UPS Measurements. UPS spectra of the perovksite films were measured on Au coated substrate. Photoelectron spectroscopy was performed in a PHI5500 Multi-Technique system using nonmonochromatized He−Iα radiation (UPS) ($h\nu$ = 21.22ev). All work function and valence-band measurement were performed at a takeoff angle of 88°, with chamber pressure near 10^{-9} Torr.

Photoluminescence Measurements. Photoluminescence (PL) measurements were performed using a Horiba Fluorolog system. Steady-state PL was collected by illuminating the samples with a monochromatized Xe lamp. Transient PL was acquired with a time-correlated single-photon-counting detector and a pulsed UV laser diode (λ = 375 nm). The instrument response function provides an overall time resolution of $\Delta t \approx$ 0.13 ns. Time-resolved emission spectra were mapped by collecting individual transient PL traces at different emission wavelengths. Absolute PL quantum yield (PLQY) measurements were done by coupling a Quanta-Phi integrating sphere to the Fluorolog system with optical fiber bundles. The measurements were done in accordance with published methods.[27] Both excitation and emission spectra were collected for the three cases of the sample directly illuminated by the excitation beam path in the integrating sphere, the sample offset within the integrating sphere from the beam path, and the empty sphere itself. The PLQY measurements were done by setting the Fluorolog to an excitation wavelength of 400 nm and to have a 5 nm bandpass for both the excitation and emission slits. With these settings, the ensuing spectra had high signal-to-noise ratios and delivered an excitation intensity in a range of 1−30 mW/cm^2 to the sample. Excitation intensity spectra were collected with a calibrated neutral density filter with known transmission placed after the integrating sphere. A Newport white light source was used to calibrate the detector and integrating sphere for spectral variance. PL spectra were collected as a function of excitation intensity by varying the slit width on the Fluorolog monochromator. The excitation intensity was calculated by measuring the power with an Ophir LaserStar Dual Channel Power and energy meter and calculating the beam area through the known dispersion relations for the monochromator.

Transient Absorption Measurements. A regeneratively amplified Yb/KGW laser at a 5 kHz repetition rate (Light Conversion, Pharos) was used to generate femtosecond laser pulses, and a pulse picker was used to lower the frequency to 1 kHz. A portion of the 1030 nm fundamental was sent into an optical bench (Ultrafast, Helios), where it passed through a retroreflector and was then focused into a calcium fluoride crystal, translated at 1 mm/s, to create the white light continuum probe. An optical parametric amplifier (Light Conversion, Orpheus) was used to generate the 350 nm pump pulse by upconversion of the fundamental wavelength. This was then sent into the optical bench and was chopped at 500 Hz. Both the pump and probe were sent to the sample, with the time delay adjusted by changing the path length of the probe (time resolution of ~350 fs). The probe pulse was then collected by a CCD after dispersion by a grating spectrograph (Ultrafast). Pump fluences were kept at 20 μJ/cm^2. Kinetic traces were fit to the convolution of the instrument response and a sum of exponential decays. Time zero was allowed to vary with wavelength to account for the chirp of the probe. All TA measurement results were plotted based on ref 28. The relative presence of each domain (Figures 2 and 3) was quantified by the amplitude of the transient absorption signal at t = 0 as

DOI: 10.1021/acs.nanolett.7b00976
Nano Lett. XXXX, XXX, XXX−XXX

$$\rho_{n_i} = \frac{\int_{n_i} \Delta A \, dE}{\int_{n} \Delta A \, dE} \quad (2)$$

Device Characterization. The luminance (L)−current density (J)−voltage (V) characteristics were collected by using a HP4140B picoammeter, a calibrated luminance meter (Konic Minolta LS-110). The absolute EL power spectra of the devices were collected with an integrating sphere and an Ocean Optics USB4000 spectrometer by the mounting of the devices on the wall of the integrating sphere. The EQE was then calculated through the measured absolute power spectra and current density.

Calculations. The procedure describing the applied stochastic Monte Carlo simulations is detailed in section S1 of the Supporting Information. The ratio of excitons and free carriers in perovskite systems has been calculated based on ref 29. The PLQY as a function of power and funnelling factor was obtained from

$$\mathrm{PLQY}(f, P_{\mathrm{pump}}) = \frac{K_{\mathrm{rad}}}{K_{\mathrm{rad}} + K_{\mathrm{trap}} + K_{\mathrm{Auger}}} \quad (3)$$

where, for simplicity, the k_{Auger} term has been included.

For flat and engineered energy landscape modeling, the energy evolution in plain landscape materials was evaluated according to the next parameters: $A = 2 \times 10^9\ \mathrm{s}^{-1}$, $B = 10^8\ \mathrm{cm}^3\ \mathrm{s}^{-1}$, and $C = 1.6 \times 10^6\ \mathrm{cm}^6\ \mathrm{s}^{-1}$, excited using a 150 fs pump excitation of 20 μJ/cm^2. For engineered energy landscape films, the individual recombination rates of the n_i domains have been kept equal to those typical of the single material.[32] A transfer rate of $k_{\mathrm{transfer}} = 10^{11}\ \mathrm{s}^{-1}$ was employed and the contribution of each domain weighted by $w = (0.6, 0.3, 0.1)$ and $w = (0.2, 0.5, 0.3)$ for the graded sample.

■ ASSOCIATED CONTENT

Supporting Information

The Supporting Information is available free of charge on the ACS Publications website at DOI: 10.1021/acs.nanolett.7b00976.

A description of Monte Carlo modeling of recombination kinetics. Figures showing a unit cell structure of perovskites; XRD, AFM, absorption, and PL analysis; UPS spectra; transient absorption data; transient PL analysis; LED characteristics; EL spectra; and LED stability. (PDF)

■ AUTHOR INFORMATION

Corresponding Authors

*E-mail: ted.sargent@utoronto.ca.
*E-mail: dhkim@ewha.ac.kr.
*E-mail: zhenghong.lu@utoronto.ca.

ORCID

Li Na Quan: 0000-0001-9301-3764
Oleksandr Voznyy: 0000-0002-8656-5074
Osman M. Bakr: 0000-0002-3428-1002
Zhenghong Lu: 0000-0003-2050-0822
Dong Ha Kim: 0000-0003-0444-0479

Author Contributions

L.N.Q., Y.Z., and F.P.G.d.A. contributed equally to this work. L.Q., Y.Z., F.P.G.A, and E.H.S. conceived the idea and proposed the experimental design. L.Q., F.P.G.A., R.S., G.W., O.V., R.C., Y.L., J.F., H.T., P.J., M.Y., and D.H.K. performed and analyzed XRD, UV absorption, PL lifetime, transient absorption, and UPS and SEM measurements. L.Q. and Y.Z. performed the device fabrication. F.P.G.A performed the simulation. L.Q., Y.Z., and Z.L. tested the devices. L.Q., F.P.G.A., O.V., and E.H.S. co-wrote the manuscript. All authors read and commented on the manuscript.

Notes

The authors declare no competing financial interest.

■ ACKNOWLEDGMENTS

This publication is based in part on work supported by award no. KUS-11-009-21, made by King Abdullah University of Science and Technology (KAUST), by the Ontario Research Fund Research Excellence Program and by the Natural Sciences and Engineering Research Council (NSERC) of Canada. L.N.Q. and D.H.K. acknowledge the financial support by National Research Foundation of Korea Grant funded by the Korean Government (2014R1A2A1A09005656 and 2015M1A2A2058365). F.P.G.d.A. acknowledges financial support from the Connaught fund.

■ REFERENCES

(1) Lee, M. M.; Teuscher, J.; Miyasaka, T.; Murakami, T. N.; Snaith, H. J. *Science* **2012**, *338*, 643−647.
(2) Burschka, J.; Pellet, N.; Moon, S.-J.; Humphry-Baker, R.; Gao, P.; Nazeeruddin, M. K.; Grätzel, M. *Nature* **2013**, *499*, 316−319.
(3) Jeon, N. J.; Noh, J. H.; Yang, W. S.; Kim, Y. C.; Ryu, S.; Seo, J.; Seok, S. I. *Nature* **2015**, *517*, 476−480.
(4) Xing, G.; Mathews, N.; Lim, S. S.; Yantara, N.; Liu, X.; Sabba, D.; Grätzel, M.; Mhaisalkar, S.; Sum, T. C. *Nat. Mater.* **2014**, *13*, 476−480.
(5) Sutherland, B. R.; Hoogland, S.; Adachi, M. M.; Wong, C. T.; Sargent, E. H. *ACS Nano* **2014**, *8*, 10947−10952.
(6) Zhu, H.; Fu, Y.; Meng, F.; Wu, X.; Gong, Z.; Ding, Q.; Gustafsson, M. V.; Trinh, M. T.; Jin, S.; Zhu, X. *Nat. Mater.* **2015**, *14*, 636−642.
(7) Tan, Z.-K.; Moghaddam, R. S.; Lai, M. L.; Docampo, P.; Higler, R.; Deschler, F.; Price, M.; Sadhanala, A.; Pazos, L. M.; Credgington, D.; et al. *Nat. Nanotechnol.* **2014**, *9*, 687−692.
(8) Hoye, R. L.; Chua, M. R.; Musselman, K. P.; Li, G.; Lai, M. L.; Tan, Z. K.; Greenham, N. C.; MacManus-Driscoll, J. L.; Friend, R. H.; Credgington, D. *Adv. Mater.* **2015**, *27*, 1414−1419.
(9) Kim, Y. H.; Cho, H.; Heo, J. H.; Kim, T. S.; Myoung, N.; Lee, C. L.; Im, S. H.; Lee, T. W. *Adv. Mater.* **2015**, *27*, 1248−1254.
(10) Cho, H.; Jeong, S.-H.; Park, M.-H.; Kim, Y.-H.; Wolf, C.; Lee, C.-L.; Heo, J. H.; Sadhanala, A.; Myoung, N.; Yoo, S.; et al. *Science* **2015**, *350*, 1222−1225.
(11) Li, G.; Tan, Z.-K.; Di, D.; Lai, M. L.; Jiang, L.; Lim, J. H.-W.; Friend, R. H.; Greenham, N. C. *Nano Lett.* **2015**, *15*, 2640−2644.
(12) Xiao, Z.; Kerner, R. A.; Zhao, L.; Tran, N. L.; Lee, K. M.; Koh, T.-W.; Scholes, G. D.; Rand, B. P. *Nat. Photonics* **2017**, *11*, 108−115.
(13) Hong, X.; Ishihara, T.; Nurmikko, A. V. *Phys. Rev. B: Condens. Matter Mater. Phys.* **1992**, *45*, 6961.
(14) Tanaka, K.; Takahashi, T.; Ban, T.; Kondo, T.; Uchida, K.; Miura, N. *Solid State Commun.* **2003**, *127*, 619−623.
(15) Yang, Y.; Yang, M.; Li, Z.; Crisp, R.; Zhu, K.; Beard, M. C. *J. Phys. Chem. Lett.* **2015**, *6*, 4688−4692.
(16) Deschler, F.; Price, M.; Pathak, S.; Klintberg, L. E.; Jarausch, D.-D.; Higler, R.; Hüttner, S.; Leijtens, T.; Stranks, S. D.; Snaith, H. J.; et al. *J. Phys. Chem. Lett.* **2014**, *5*, 1421−1426.
(17) Stranks, S. D.; Burlakov, V. M.; Leijtens, T.; Ball, J. M.; Goriely, A.; Snaith, H. J. *Phys. Rev. Appl.* **2014**, *2*, 034007.
(18) Saparov, B.; Mitzi, D. B. *Chem. Rev.* **2016**, *116*, 4558−96.
(19) Quan, L. N.; Yuan, M.; Comin, R.; Voznyy, O.; Beauregard, E. M.; Hoogland, S.; Buin, A.; Kirmani, A. R.; Zhao, K.; Amassian, A.; et al. *J. Am. Chem. Soc.* **2016**, *138*, 2649−2655.

DOI: 10.1021/acs.nanolett.7b00976
Nano Lett. XXXX, XXX, XXX−XXX

(20) Yu, J. C.; Kim, D. W.; Kim, D. B.; Jung, E. D.; Park, J. H.; Lee, A. Y.; Lee, B. R.; Di Nuzzo, D.; Friend, R. H.; Song, M. H. *Adv. Mater.* **2016**, *28*, 6906−6913.
(21) Mitzi, D. B.; Feild, C.; Harrison, W.; Guloy, A. *Nature* **1994**, *369*, 467−469.
(22) Sichert, J. A.; Tong, Y.; Mutz, N.; Vollmer, M.; Fischer, S.; Milowska, K. Z.; García Cortadella, R.; Nickel, B.; Cardenas-Daw, C.; Stolarczyk, J. K.; et al. *Nano Lett.* **2015**, *15*, 6521−6527.
(23) Milot, R. L.; Sutton, R. J.; Eperon, G. E.; Haghighirad, A.-A.; Martinez Hardigree, J. F.; Miranda, L.; Snaith, H. J.; Johnston, M. B.; Herz, L. M. *Nano Lett.* **2016**, *16*, 7001−7007.
(24) Wang, N.; Cheng, L.; Ge, R.; Zhang, S.; Miao, Y.; Zou, W.; Yi, C.; Sun, Y.; Cao, Y.; Yang, R. *Nat. Photonics* **2016**, *10*, 699−704.
(25) Byun, J.; Cho, H.; Wolf, C.; Jang, M.; Sadhanala, A.; Friend, R. H.; Yang, H.; Lee, T. W. *Adv. Mater.* **2016**, *28*, 7515−7520.
(26) Yuan, M.; Quan, L. N.; Comin, R.; Walters, G.; Sabatini, R.; Voznyy, O.; Hoogland, S.; Zhao, Y.; Beauregard, E. M.; Kanjanaboos, P.; et al. *Nat. Nanotechnol.* **2016**, *11*, 872−877.
(27) Wu, X.; Trinh, M. T.; Niesner, D.; Zhu, H.; Norman, Z.; Owen, J. S.; Yaffe, O.; Kudisch, B. J.; Zhu, X.-Y. *J. Am. Chem. Soc.* **2015**, *137*, 2089−2096.
(28) Sum, T. C.; Mathews, N.; Xing, G.; Lim, S. S.; Chong, W. K.; Giovanni, D.; Dewi, H. A. *Acc. Chem. Res.* **2016**, *49*, 294−302.
(29) Manser, J. S.; Kamat, P. V. *Nat. Photonics* **2014**, *8*, 737−743.
(30) Jeon, N. J.; Noh, J. H.; Kim, Y. C.; Yang, W. S.; Ryu, S.; Seok, S. I. *Nat. Mater.* **2014**, *13*, 897−903.
(31) Berera, R.; van Grondelle, R.; Kennis, J. T. *Photosynth. Res.* **2009**, *101*, 105−118.
(32) Rowland, C. E.; Fedin, I.; Zhang, H.; Gray, S. K.; Govorov, A. O.; Talapin, D. V.; Schaller, R. D. *Nat. Mater.* **2015**, *14*, 484−489.

DOI: 10.1021/acs.nanolett.7b00976
Nano Lett. XXXX, XXX, XXX−XXX